Difference Solution of a Viscous Flow with Free-Surface Wave about an Advancing Ship

HIDEAKI MIYATA, TORU SATO, AND NOBUHIRO BABA

Department of Naval Architecture, University of Tokyo, Tokyo, Japan

Received March 26, 1986; revised November 17, 1986

A finite-difference solution method is described for a 3D viscous flow with free-surface waves about an advancing ship in steady course. A Navier–Stokes equation of finite-difference form is solved by a time-marching scheme in a boundary-fitted curvilinear coordinate system which is deformed to fit the moving free-surface at each time step. A sub-grid-scale turbulence model is introduced to achieve computations at higher Reynolds numbers. It is demonstrated that the computations by this method simulate fairly well free-surface waves, viscous flows and their interactions including three-dimensional separation under the influence of the free-surface. © 1987 Academic Press, Inc

CONTENTS. 1. Introduction. 2. Boundary-fitted Coordinate System. 3. Governing Equations. 3.1. Navier–Stokes equation in rotational form. 3.2. Navier–Stokes equation in a moving grid system. 4. Turbulence Model. 4.1. SGS stresses. 4.2. SGS stress terms in curvilinear coordinates. 4.3. Nondimensionalization. 5. Computational Procedure. 5.1 Solution algorithm. 5.2. Finite-difference approximation. 6. Boundary Conditions. 6.1. Free-surface condition. 6.2. Filtering of free-surface. 6.3. Other boundary conditions. 7. Computed Results. 7.1. Condition of computation. 7.2. Effect of Reynolds number. 7.3. Wave formation and pressure distribution on ship surface. 7.4. Flow field. 8. Concluding Remarks.

1. INTRODUCTION

As is well known, a ship advancing on a steady course generates a viscous flow field as well as a wave field, and these flow fields render viscous and wave resistance forces on it, respectively. Although these two flow fields and two resultant resistance components have intimate mutual interactions, they have long been separately studied both experimentally and theoretically.

Laboratory experiments with ship models are used to perform in accordance with Froude's law of similarity. In the usual resistance tests the wave resistance is derived by empirically extracting the viscous resistance from the total resistance of a model ship at a relatively lower Reynolds number than a full-scale ship. This procedure of experiment, which has been commonly applied for more than a hundred years, contains fundamental uncertainty. Furthermore, the nonlinear properties of ship waves which have been elucidated in the last decade [1] and the interactions of a viscous flow with waves, especially at the stern [2, 3], make the fluid motion much more complicated.

Theoretical investigations on the viscous flow about a ship have long been based on the boundary layer theory which cannot explain the viscous flow after separation. Recently partially parabolic equations are used for the numerical calculations of the viscous flow on and after a ship, e.g., Chen and Patel [4]. A new attempt to solve the Navier–Stokes (NS) equation is made by Kodama [5]. However, the simplification of the governing equations may give limitations to the fluid motions in the former and similar methods, and the degree of accuracy of the latter method does not seem to be sufficient. Furthermore, the presence of the free-surface is not considered and the availability of the turbulence model is not well examined in either method.

A finite-difference method based on the NS-equation is used for the simulation of ship waves by Miyata et al. [6, 7]. Although the agreement in wave geometry is satisfactory, the viscous flow is not solved due to the use of a rectangular inflexible mesh system and an insufficient degree of accuracy of the difference scheme.

To achieve numerical simulation of the complicated viscous flow at the stern with wave motion, postulations or approximations must be reduced to the minimum, since they may contaminate the solution. A finite-difference method based on the NS-equation with a proper turbulence model seems to be most suitable for this kind of problem. A two-equation model, the so-called $K - \varepsilon$ model, is often used recently. However, it seems very arbitrary with respect to the initial condition and too many empirical constants. Furthermore, this model is not considered capable of simulating a separated flow. Another model called sub-grid-scale model which is used in large-eddy simulations seems to have more versatile properties, having simple equations and the least number of empirical constants. More realistic simulation of a viscous flow about a body of arbitrary configuration is expected with this model if a sufficiently fine cell system is available. It appears safe to say that developing a computational method of the large-eddy simulation type for a flow about an arbitrary body provides the first important step for completion of a computational experimental tank. Second, the shortage of sufficient computer storage now available will be resolved in the near future.

For the solution of the viscous flow about a ship, a boundary-fitted curvilinear coordinate system must be employed and a higher degree of accuracy is necessary. To explain wave motion, particular techniques are necessary so that the nonlinear free-surface conditions are implemented on the moving boundary. In this paper the boundary-fitted curvilinear coordinate system is generated by solving an elliptic partial differential system at every time step of the time-marching. The NS-equation in rotational form, which conserves both momentum and kinetic energy, is used and a sub-grid-scale turbulence model is incorporated. The computer code is written in a form suitable for a supercomputer, namely for a vector processor. In Section 2 the generation of a boundary-fitted coordinate system is briefly described. The governing equations in a moving coordinate system and the turbulence model are described in Sections 3 and 4. The computational procedure and the finite-difference scheme are explained in Section 5. The method to implement the nonlinear free-surface condition by moving the grid system and other boundary

conditions, which are also very important, are described in Section 6. Some computed results on a variety of conditions, with and without waves, at three Reynolds numbers and at three Froude numbers, are presented and discussed in Section 7. Brief concluding remarks are mentioned in Section 8.

2. BOUNDARY-FITTED COORDINATE SYSTEM

The method proposed by Thompson *et al.* [10–12] is used for the generation of a boundary-fitted curvilinear coordinate system. The physical region G in x^1 x^2 x^3-space bounded by arbitrary-shaped boundaries ∂G is transformed to the rectangular region H in ξ^1 ξ^2 ξ^3-space as seen in Fig. 1. Since the configuration of a ship is symmetrical and the flow is also assumed to be approximately symmetrical, only one side of a ship is considered.

The coordinates in the physical region are expressed as a function of the coordinates in the transformed region as

$$x^i = x^i(\xi^1, \xi^2, \xi^3). \tag{1}$$

To determine the smooth function for Eq. (1), the following elliptic partial differential equation is solved by a successive relaxation method:

$$g^{ij} \frac{\partial^2 x^n}{\partial \xi^i \partial \xi^j} + \frac{\psi^i \partial x^n}{\partial \xi^i} = 0, \tag{2}$$
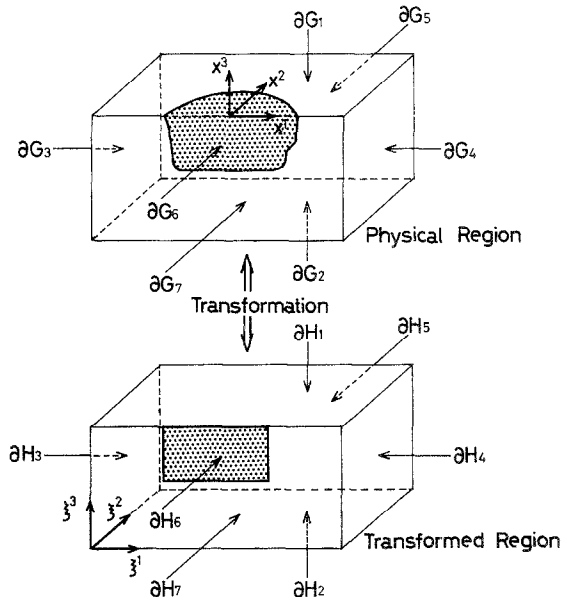

FIG. 1. Transformation of the computational domain.

MIYATA, SATO, AND BABA

TABLE I

Boundary Conditions for Grid Generation

Boundaries	Dirichlet condition			Neumann condition		
∂H_1 Free-surface	x^1	x^2	x^3			
∂H_2 Bottom			x^3	x^1	x^2	
∂H_3 Inflow	x^1	x^2	x^3			
∂H_4 Outflow	x^1				x^2	x^3
∂H_5 Side		x^2		x^1		x^3
∂H_6 Ship surface		x^2		x^1		x^3
∂H_7 Centerplane		x^2		x^1		x^3

where

$$\psi^i = \overline{A^i}\,\text{sgn}(\overline{\xi^i} - \xi^i)\exp(-\overline{B^i}\,|\overline{\xi^i} - \xi^i|). \tag{3}$$

Here A and B are attraction and decay factors, respectively, and $\xi^i = \overline{\xi^i}$ denotes the specified coordinate surface to which coordinate surfaces of $\xi^i = \text{const}$ are attracted. The values of A and B are described in the subsequent section. On the seven boundaries, the Dirichlet or Neumann condition, the latter of which means that the derivatives approximately normal to the boundary are set at zero, is imposed as listed in Table I. An example of a generated grid system is shown in Fig. 2.
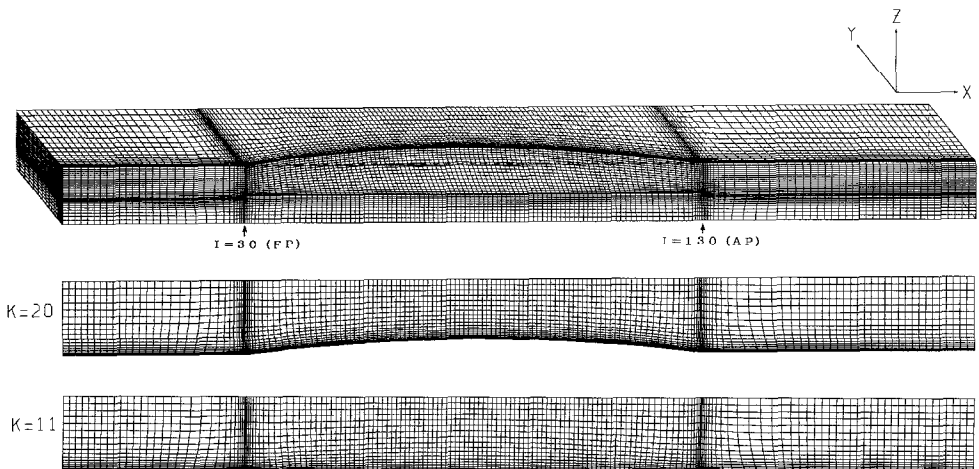

FIG. 2. Initial grid system.

The metric tensors are defined by

$$g_{ij} = \frac{\partial x^k}{\partial \xi^i} \frac{\partial x^l}{\partial \xi^j} \delta_{kl},$$ (4a)

$$g = \det(g_{ij}),$$ (4b)

$$g^{ij} = \tfrac{1}{2} g^{-1} e^{imn} e^{jpq} g_{mp} g_{nq}.$$ (4c)

where δ and e denote the Kronecker delta and the Eddington permutation symbol, respectively. The metric tensor is used hereafter to describe the computational method, since we solve directly three curvilinear components of the velocity vector and a pressure scalar in the curvilinear coordinate system, in which both dependent and independent variables are curvilinear. Thus the present method differs from the previous work by Shanks and Thompson [12].

3. Governing Equations

3.1. Navier–Stokes Equation in Rotational Form

The following NS-equation and the equation of continuity are the governing equations:

$$\frac{\partial \mathbf{u}}{\partial t} = -\mathbf{grad}(P + \tfrac{1}{2}\mathbf{u} \cdot \mathbf{u} + g_r x^3) + \mathbf{u} \times \mathbf{rot}(\mathbf{u}) - v \cdot \mathbf{rot}(\mathbf{rot}(\mathbf{u})),$$ (5)

$$\mathrm{div}(\mathbf{u}) = 0.$$ (6)

Here, $\mathbf{u}$ is the velocity vector, t is the time, P is the pressure divided by the density, v is the kinematic viscosity, and g_r is the gravitational acceleration. This rotational form of the NS-equation has the advantage of having the conservative property for both momentum and kinetic energy. Furthermore, this formulation makes the representation in general curvilinear coordinates very simple without involving Christoffel symbols that may arise from the covariant differentiation of a vector or a higher-order tensor. Denoting the general curvilinear coordinates by ξ^i and, using the metric tensor g_{ij}, its determinant g, and its conjugated tensor g^{ij}, the following governing equations in general curvilinear coordinates are derived:

$$\frac{\partial u^i}{\partial t} = -g^{ij} \frac{\partial}{\partial \xi^j} (P + \tfrac{1}{2} g_{kl} u^k u^l + g_r x^3) + g^{ij} \varepsilon_{jkl} u^k \omega^l$$

$$- v \varepsilon^{ijk} \frac{\partial}{\partial \xi^j} (g_{kl} \omega^l),$$ (7)

$$g^{-1/2} \frac{\partial}{\partial \xi^i} (g^{1/2} u^i) = 0,$$ (8)

where ε^{ijk} is a third-order tensor and refers to the Eddington permutation symbol e as

$$\varepsilon^{ijk} = g^{-1/2} e^{ijk}, \tag{9}$$

and ω is a contravariant vector of vorticity defined as

$$\omega^i \equiv \varepsilon^{ijk} \frac{\partial}{\partial \xi^j} (g_{kl} u^l). \tag{10}$$

3.2. Navier–Stokes Equation in a Moving Grid System

Since the free-surface is deformed due to the wave generation in the time-marching solution procedure, the general curvilinear coordinates must move so that the uppermost coordinate surface fits this free-surface boundary. Therefore, the coordinates ξ^i is a function of not only the Cartesian coordinates x^i but also time t. Then the time-derivative term of the NS-equation in time-dependent curvilinear coordinates becomes [13]

$$\frac{\partial \mathbf{u}}{\partial t(x^i)} = \frac{\partial \mathbf{u}}{\partial t(\xi^j)} + (\mathbf{grad\ u}) \cdot \mathbf{v}. \tag{11}$$

Here, $\mathbf{v}$ is the velocity vector of the movement of the grid points and is defined as

$$\mathbf{v} = \frac{\partial \xi^i}{\partial t} \mathbf{g}_{(i)}. \tag{12}$$

Here, $\mathbf{g}_{(i)}$ is a base vector in the curvilinear coordinate system. By substituting a position vector $\mathbf{r}$ for $\mathbf{u}$ in Eq. (11) another definition of the velocity vector of the moving grid points is derived as

$$\mathbf{v} = -\frac{\partial \mathbf{r}}{\partial t(\xi^j)}; \tag{13}$$

Eq. (12) is a representation with reference to the fixed coordinates and Eq. (13) with reference to the moving coordinates. Then Eq. (11) is deformed as

$$\frac{\partial \mathbf{u}}{\partial t(x^i)} = \frac{\partial \mathbf{u}}{\partial t(\xi^j)} + \mathrm{div}(\mathbf{uv}) - \mathbf{u}\ \mathrm{div}\ \mathbf{v}. \tag{14}$$

Since the divergence of the velocity vector $\mathbf{v}$ with reference to the moving coordinates is given as

$$\mathrm{div}\ \mathbf{v} \equiv g^{-1/2} \frac{\partial}{\partial \xi^i} (g^{1/2} v^i)$$

$$= -g^{-1/2} \frac{\partial g^{1/2}}{\partial t}, \tag{15}$$

the first and third terms of Eq. (14) are written as

$$\frac{\partial \mathbf{u}}{\partial t} - \mathbf{u}\,\mathrm{div}\,\mathbf{v} = \frac{\partial \mathbf{u}}{\partial t} + \mathbf{u}g^{-1/2}\frac{\partial g^{1/2}}{\partial t}$$

$$= g^{-1/2}\frac{\partial}{\partial t}(g^{1/2}\mathbf{u}). \tag{16}$$

Then, the following NS-equation in a moving coordinate system is obtained, keeping the rotational form,

$$g^{-1/2}\frac{\partial}{\partial t}(g^{1/2}\mathbf{u}) = -\,\mathbf{grad}(P + \tfrac{1}{2}\mathbf{u}\cdot\mathbf{q} + g_r x^3)$$

$$+ \tfrac{1}{2}\{\mathbf{q}\times\mathbf{rot}(\mathbf{u}) + \mathbf{u}\times\mathbf{rot}(\mathbf{q}) - \mathbf{rot}(\mathbf{u}\times\mathbf{q}) - \mathbf{u}\,\mathrm{div}\,\mathbf{v}\}$$

$$- v\,\mathbf{rot}(\mathbf{rot}(\mathbf{u})), \tag{17}$$

where

$$\mathbf{q} = \mathbf{u} + \mathbf{v} \tag{18}$$

is the modified velocity. In general curvilinear coordinates Eq. (17) is written as

$$g^{-1/2}\frac{\partial}{\partial t}(g^{1/2}u^i\mathbf{g}_{(i)}) = a^i\mathbf{g}(i), \tag{19a}$$

$$a^i = -g^{ij}\frac{\partial}{\partial\xi^j}(P + \tfrac{1}{2}g_{kl}u^k q^l + g_r x^3)$$

$$+ \frac{1}{2}\left[g^{ij}\varepsilon_{jkl}q^k\omega^l + g^{ij}\varepsilon_{jkl}u^k\left\{\varepsilon^{lmn}\frac{\partial}{\partial\xi^m}(g_{ns}q^s)\right\}\right.$$

$$\left. - \varepsilon^{ijk}\frac{\partial}{\partial\xi^j}(\varepsilon_{kmn}u^m q^n) - u^i g^{-1/2}\frac{\partial}{\partial\xi^j}(g^{1/2}v^j)\right]$$

$$- v\varepsilon^{ijk}\frac{\partial}{\partial\xi^j}(g_{kl}\omega^l). \tag{19b}$$

where

$$\omega^l \equiv \varepsilon^{lmn}\frac{\partial}{\partial\zeta^m}(g_{ns}u^s). \tag{20}$$

A scalar form of velocity is derived by the following transformation with a base vector in the Cartesian coordinates i, which is convenient in the time-marching procedure described in the subsequent section.

$$\mathbf{g}_{(i)} = \frac{\partial x^k}{\partial\xi^i}\mathbf{i}_{(k)}. \tag{21}$$

4. TURBULENCE MODEL

4.1. *SGS Stresses*

A sub-grid-scale (SGS) turbulence model is employed following Deardorff [8]. In partial analogy to the molecular case the SGS stress R^{ij} is expressed as

$$R^{ij} \equiv \overline{u''^i u''^j} = \tfrac{1}{3} g^{ij} \, \overline{u''^l u''^m} \, g_{lm} - 2 v_s \, \overline{e^{ij}}. \tag{22}$$

Here, the primes denote deviations from local grid-volume means and the overbars are grid-scale averaging operators, v_s is the SGS eddy viscosity coefficient, $\overline{e_{ij}}$ is defined as

$$\overline{e_{ij}} = \tfrac{1}{2}(\overline{u_{i;j}} + \overline{u_{j;i}}), \tag{23}$$

where the subscript with a symbol ";" denotes a covariant derivative with respect to the subscript.

The dimensional arguments demand that

$$v_s = (C_0 \, \Delta)^{4/3} \, E^{1/3}, \tag{24}$$

where

$$\Delta \equiv (\Delta x \cdot \Delta y \cdot \Delta z)^{1/3} = g^{1/6}. \tag{25}$$

The rate of dissipation of the turbulent kinetic energy within a local grid volume E is approximately given by

$$E = v_s \, 2\overline{e_{ij}} \, \overline{e^{ij}}. \tag{26}$$

Then the Smagorinsky *et al.* [9] assumption for v_s is derived as

$$v_s = (C_0 \, \Delta)^2 \, (2\overline{e_{ij}} \, \overline{e^{ij}})^{1/2}. \tag{27}$$

The empirical coefficient C_0 is set at 0.1.

The first term of Eq. (22) is the turbulent kinetic energy K multiplied by $\tfrac{2}{3}$. From the dimensional arguments

$$v_s = CK^2/E, \tag{28}$$

then Eqs. (24) and (28) give

$$\frac{1}{3} \overline{u''^l u''^m} \, g_{lm} \equiv \frac{2}{3} K = \frac{2}{3} \frac{v_s^2}{(C_1 \, \Delta)^2}. \tag{29}$$

The coefficient C_1 is set at 0.094 following Deardorff [8].

4.2. SGS Stress Terms in Curvilinear Coordinates

In order to introduce the SGS stresses into the NS-equation, the covariant derivative of R^{ij} is required:

$$R^{ij}{}_{,j} = \tfrac{2}{3} K_{,j} g^{ij} - 2v_s e^{ij}{}_{,j} - 2v_{s,j} e^{ij}. \tag{30}$$

It is noted that the overbars denoting averaging operations are used only in Section 4.1 and they are dropped in this and succeeding sections for simplicity. The first term can be treated together with the pressure in the NS-equation. The second term is deformed into a form similar to the viscous diffusion term of the NS-equation as follows:

$$-2v_s e^{ij}{}_{,j} = -v_s g^{jm} u^i{}_{,mj}$$

$$= v_s \varepsilon^{ijk} \frac{\partial}{\partial \xi^j} (g_{kl} \omega^l). \tag{31}$$

Therefore, the NS-equation with the SGS turbulence model in the general curvilinear coordinate system is from Eqs. (19), (29), and (31):

$$g^{-1/2} \frac{\partial}{\partial t} (g^{1/2} u^i \mathbf{g}_{(i)}) = a^i \mathbf{g}_{(i)}, \tag{32a}$$

$$a^i = -g^{ij} \frac{\partial}{\partial \xi^j} (P + \tfrac{1}{2} g_{kl} u^k q^l + g_r x^3 + \tfrac{2}{3} K)$$

$$+ \tfrac{1}{2} \left[g^{ij} \varepsilon_{jkl} q^k \omega^l + g^{ij} \varepsilon_{jkl} u^k \left\{ \varepsilon^{lmn} \frac{\partial}{\partial \xi^m} (g_{ns} q^s) \right\} \right.$$

$$\left. - \varepsilon^{ijk} \frac{\partial}{\partial \xi^j} (\varepsilon_{kmn} u^m q^n) - u^i g^{-1/2} \frac{\partial}{\partial \xi^j} (g^{1/2} v^j) \right]$$

$$- (v + v_s) \varepsilon^{ijk} \frac{\partial}{\partial \xi^j} (g_{kl} \omega^l) + 2 \frac{\partial v_s}{\partial \xi^j} e^{ij}. \tag{32b}$$

The deformation tensor e_{ij} and e^{ij} in Eqs. (26) and (31) are calculated using the following relations:

$$2e_{ij} = u_{i;j} + u_{j;i}$$

$$= g_{ik} \frac{\partial u^k}{\partial \xi^j} + g_{jk} \frac{\partial u^k}{\partial \xi^i} + \frac{\partial g_{ij}}{\partial \xi^l} u^l, \tag{33}$$

$$e^{ij} = g^{il} g^{jk} e_{lk}. \tag{34}$$

4.3. Nondimensionalization

When variables are made dimensionless as

$$\mathbf{r}' = \mathbf{r}/L, \quad \mathbf{u}' = \mathbf{u}, \quad P' = P/U^2, \quad K' = K/U^2, \quad t' = t/(L/U), \tag{35}$$

where L is the ship length and U is the advance speed, and the primes are dropped for simplicity, the first, third, and last terms of Eq. (32b) become, respectively,

$$-g^{ij}\frac{\partial}{\partial\xi^j}(P+\tfrac{1}{2}g_{kl}u^kq^l+F^{-2}x^3+\tfrac{2}{3}K), \tag{36a}$$

$$-\frac{1}{R_t}\varepsilon^{ijk}\frac{\partial}{\partial\xi^j}(g_{kl}\omega^l), \tag{36b}$$

$$2\frac{\partial R_s^{-1}}{\partial\xi^j}e^{ij}. \tag{36c}$$

Here, F is the Froude number and R_t and R_s are the Reynolds numbers defined as

$$F=U/\sqrt{g_r L}, \tag{37a}$$

$$R_t=UL/(v+v_s), \tag{37b}$$

$$R_s=UL/v_s. \tag{37c}$$

5. Computational Procedure

5.1. *Solution Algorithm*

By forward differencing in time the NS-equation (32) with Eq. (36) becomes

$$g^{-1/2}\frac{g^{(1/2)}\overset{(n+1)(n+1)}{\mathbf{u}}}{\varDelta t}=-\text{grad }\phi+\mathbf{b}. \tag{38}$$

Here, ϕ is the sum of the scalar quantity shown in the parentheses of Eq. (36a), $\mathbf{b}$ is the sum of all other terms including $\mathbf{u}/\varDelta t$. The superscript $(n+1)$ denotes the time level and n is dropped for simplicity. Taking the divergence of Eq. (38) and letting the divergence at the $(n+1)$th time step be zero by Eq. (8), we have a Poisson equation for the Bernoulli scalar ϕ as

$$g^{-1/2}\frac{\partial}{\partial\xi^i}\left(g^{1/2}g^{ij}\frac{\partial\phi}{\partial\xi^j}\right)=g^{-1/2}\frac{\partial}{\partial\xi^i}(g^{1/2}b^i). \tag{39}$$

Therefore, we have the computational procedure as follows. First a solenoidal velocity field is given as an initial condition:

$$u^i=0. \tag{40}$$

The fluid motion is initiated by giving an acceleration of a flow to the term $\mathbf{b}$ of

Eq. (38). In this new velocity field the Bernoulli scalar field is iteratively calculated through the following equation which is derived from Eq. (39):

$$\overset{(m+1)}{\phi} = \overset{(m)}{\phi} + \alpha g^{-1/2} \frac{\partial}{\partial \xi^i} \left\{ g^{1/2} \left(g^{ij} \frac{\partial \overset{(m)}{\phi}}{\partial \xi^j} - b^i \right) \right\}. \tag{41}$$

Here, α is a relaxation factor and the superscript m denotes the iterative level. The velocity vector is renewed by the new scalar field through Eq. (32) and the difference of the base vector $\mathbf{g}(i)$ due to the time-marching is considered by once transforming the velocity components onto the Cartesian coordinates using Eq. (21).

The free-surface configuration is deformed by the movement of the grid points following the free-surface conditions described in the subsequent section. The new grid system is generated by solving Eq. (2) under the updated boundary conditions. Then the new Bernoulli quantity field is obtained by Eq. (41) and the cycle is repeated until the acceleration of the flow ceases and a sufficiently steady state is reached.

5.2. *Finite-Difference Approximation*

The difference form of the NS-equation in rotational form retains its property of conserving the kinetic energy when a symmetrical differencing scheme is used. Among a number of differencing schemes the second-order centered differencing and the fourth-order compact differencing are well known as symmetrical schemes. In this study the second-order centered differencing scheme is used for space differencing, since the fourth-order compact scheme requires remarkable computation time. The space differencing for the Poisson equations (2) and (39) for the solution of a grid system and for the solution of a pressure field, respectively, also uses the second-order centered differencing.

6. Boundary Conditions

6.1. *Free-Surface Condition*

The free-surface boundary conditions appropriate for the NS-equation are one kinematic and two dynamic conditions. The latter means that the normal and tangential stresses vanish. These stress conditions must be carefully implemented in a strict sense. However, the viscous stresses are ignored in this study, since it is safely accepted that the role of viscous stresses is almost negligible and the viscous layer is ultimately thin on the free-surface in the present problem of a high Froude number flow. Therefore, the normal stress condition becomes the simplest one that gives the atmospheric pressure on the free-surface and the tangential stress condition disappears.

As shown in Table II, another boundary condition of zero-normal gradient for the velocity vectors is imposed at the free-surface. This condition is derived from the

TABLE II

Boundary Conditions for the Solution Procedure

Boundaries		Bernoulli scalar ϕ	Velocity vector $\mathbf{u}$
Free-surface	$\xi^3_{\max}$	$P = P_{\text{air}} \approx 0$	$\mathbf{u}(\xi^3_{\text{MAX}}) = \mathbf{u}(\xi^3_{\text{MAX}-1})$
Bottom	ξ^3_1	$P + F^{-2}X^3$	$\mathbf{u}(\xi^3_1) = \mathbf{u}(\xi^3_2)$
Inflow	ξ^1_1	$P + F^{-2}X^3$	Uniform flow
Outflow	ξ^1_{MAX}	$\phi(\xi^1_{\text{MAX}}) = \phi(\xi^1_{\text{MAX}-1})$	$\mathbf{u}(\xi^1_{\text{MAX}}) = \mathbf{u}(\xi^1_{\text{MAX}-1})$
Side	ξ^2_{MAX}	$\phi(\xi^2_{\text{MAX}}) = \phi(\xi^2_{\text{MAX}-1})$	$\mathbf{u}(\xi^2_{\text{MAX}}) = \mathbf{u}(\xi^2_{\text{MAX}-1})$
Ship surface	ξ^2_2	$\phi(\xi^2_1) = \phi(\xi^2_3) - 2a^2(\xi^2_2)$	$\mathbf{u}(\xi^2_2) = 0$
Centerplane	ξ^2_2	$\phi(\xi^2_1) = \phi(\xi^2_3)$	$\|\mathbf{u}(\xi^2_1)\| = \|\mathbf{u}(\xi^2_3)\|$

Note. Subscripts for ξ denote number of grid point.

above tangential stress condition, assuming that the curvature of the surface is small and the tangential gradient of the normal velocity is small. This condition is very appropriate when the vertical spacing of the grid system is so fine that the viscous layer on the free-surface is resolved. However, it is almost impossible to resolve it in this study due to limited computer storage. Therefore the zero-normal-gradient condition for the velocity vectors is employed simply from the stability point of view for the time being, which is necessary partly by the use of the backward differencing of velocities at the free-surface. This nominal tangential stress condition may deteriorate the accuracy unless fine spacing is used in the proximity of the free-surface.

The kinematic condition is implemented by the movement of the uppermost curvilinear surface, as described in detail below.

According to experimental investigation [1] the slope of the free-surface caused by the advancing motion of a ship sometimes reaches 60° to the horizontal surface. However, it is usually within 30° and it has been demonstrated already that the representation of the free-surface location as a single-valued function of (x^1, x^2) gives satisfactory agreement with measurement [7]. For further advanced study, the resolution of breaking free-surface motion seems to be of significant importance. The authors have previously worked on the numerical simulation of breaking waves in two dimensions [17]. However, we still have a lot of difficulty achieving simulations of three-dimensional breaking motion.

The kinematic condition implies that fluid particles on the free-surface remain on it. Assume that the wave height in the physical region is

$$x^3 = f(x^1, x^2, t), \tag{42}$$

then the kinematic condition becomes

$$\frac{\partial f}{\partial t} + \frac{\partial f}{\partial x^1}\frac{dx^1}{dt} + \frac{\partial f}{\partial x^2}\frac{dx^2}{dt} - \frac{dx^3}{dt} = 0. \tag{43}$$

The velocity terms dx^i/dt in Eq. (43) are defined in the Cartesian coordinates as

$$\frac{dx^i}{dt} \equiv u^{i*}. \tag{44}$$

In the transformed region the plane of constant ξ^3 represents the free-surface and in the physical region the uppermost coordinate of x^3 which is a function of (ξ^1, ξ^2, ξ^3) represents the free-surface. Therefore, the kinematic free-surface condition becomes

$$\frac{\partial x^3}{\partial t} = u^{3*} - \left\{ \frac{\partial x^3}{\partial \xi^1} \frac{\partial \xi^1}{\partial x^1} + \frac{\partial x^3}{\partial \xi^2} \frac{\partial \xi^2}{\partial x^1} \right\} u^{1*}$$

$$- \left\{ \frac{\partial x^3}{\partial \xi^1} \frac{\partial \xi^1}{\partial x^2} + \frac{\partial x^3}{\partial \xi^2} \frac{\partial \xi^2}{\partial x^2} \right\} u^{2*}. \tag{45}$$

When the velocity field is determined at every time step, the grid points that represent the free-surface are moved by Eq. (45) in an Eulerian manner. This gives the free-surface configuration and the grid system is renewed by solving Eq. (2) under this new Dirichlet condition for x^3.

The dynamic condition is satisfied by simply giving the atmospheric pressure to P of the scalar quantity ϕ in Eq. (39) on the free-surface.

6.2. Filtering of the Free-Surface

The free-surface configuration sometimes shows fluctuations of which a wavelength is equal to two grid spacings. In order to remove this unfavorable fluctuation, filtering is applied to the free-surface coordinates, updated by Eq. (45).

Assume that a local wave profile in the directions of ξ^1 or ξ^2 is expressed by a quadratic equation and it contains a triangular-shaped fluctuation, then the wave height h is written as [14]

$$h(x) = (a_0 + a_1 x + a_2 x^2) + (-1)^j (b_0 + b_1 x). \tag{46}$$

We use five points for the filtering equation,

$$\bar{h}(x_j) = c_{j-2} h(x_{j-2}) + c_{j-1} h(x_{j-1}) + c_j h(x_j) + c_{j+1} h(x_{j+1}) + c_{j+2} h(x_{j+2}). \tag{47}$$

To eliminate the terms with the coefficients of b_0 and b_1 from the filtered wave height h, the coefficients in Eq. (47) must be

$$c_{j-2} = (\Delta x_{j+1} \Delta x_{j-1})/\{2(\Delta x_{j-2} - \Delta x_{j+2}) \Delta x_{j-2}\},$$

$$c_{j-1} = \Delta x_{j+1}/\{2(\Delta x_{j+1} - \Delta x_{j-1})\},$$

$$c_j = (\Delta x_{j+2} \Delta x_{j-2} - \Delta x_{j+1} \Delta x_{j-1})/(2\Delta x_{j+2} \Delta x_{j-2}), \tag{48}$$

$$c_{j+1} = \Delta x_{j-1}/\{2(x_{j-1} - \Delta x_{j+1})\},$$

$$c_{j+2} = \Delta x_{j+1} \Delta x_{j-1}/\{2(\Delta x_{j+2} - \Delta x_{j-2}) \Delta x_{j+2}\},$$

where

$$\Delta x_{j-2} = x_{j-2} - x_j, \qquad \Delta x_{j-1} = x_{j-1} - x_j,$$
$$\Delta x_{j+1} = x_{j+1} - x_j, \qquad \Delta x_{j+2} = x_{j+2} - x_j. \tag{49}$$

It is demonstrated in previous works [6, 14] that the presumable dissipative property of this filtering does not seriously influence the solution. This filtering is made in the directions of both ξ^1 and ξ^2. The grid system deformed by the movement of the free-surface in the manner described above is shown in Fig. 3.

6.3. Other Boundary Conditions

Special treatment of the free-surface location must be introduced at the intersection of the free-surface with the hull so that the singularity is removed. First, the wave height is extrapolated from the two outer values using Eq. (47) with a symmetry condition. Let us assume x_j is the coordinate of the intersection and x_{j+1} and x_{j+2} are outer points where the wave height is normally computed, and set the wave height at the inner points x_{j-1} and x_{j-2} equal to the outer values symmetrically. Then Eq. (47) is modified as

$$(1 - c_j)\, h(x_j) = 2\{c_{j+1} h(x_{j+1}) + c_{j+2} h(x_{j+2})\}. \tag{50}$$

It is noted that an alternative extrapolation method for giving the same value, with x_{j+1} at the intersection x_j, leads to divergence of the solution. Second, the (x^1, x^2) coordinates of this point are moved to coincide with the exact hull surface. These approximations at the intersection do not seem to be a source of serious error, since a very fine spacing is used near both the free-surface and the hull surface and the time increment is very small.

Boundary conditions for the Bernoulli quantity (or pressure) and the velocities are listed in Table II. Hydrostatic pressure is assumed on the inflow and bottom boundaries where the influence of the fluid motion due to an advancing ship is nearly negligible. The pressure on the ship surface is normally computed with the inner pressure extrapolated by the relation of the NS-equation shown in Table II. The NS-equation gives three conditions for ϕ[18] and one in the ξ^2-direction,
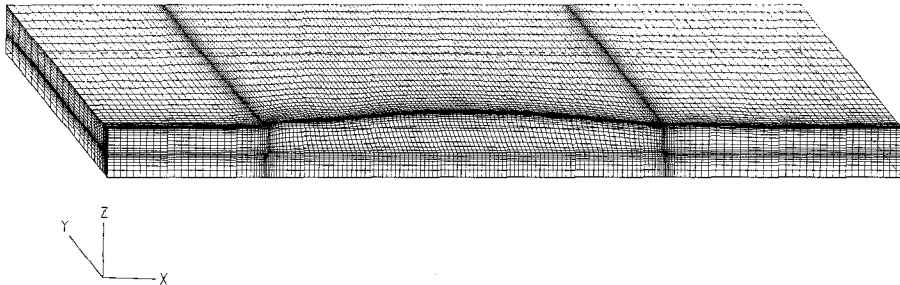

FIG. 3. Grid system deformed by waves.

which is nearly normal to the ship surface, is taken here. This treatment of the pressure condition on a body surface was tested by the authors in the previous work [16]. At a number of boundaries a very simple boundary condition of no-gradient for variables in the direction approximately normal to the boundaries is imposed. The Bernoulli scalar quantities are equally set at the outflow and side boundaries, and the velocity vectors are extrapolated in the same manner at the free-surface, bottom, outflow, and side boundaries as shown in Table II. The error due to these approximations is reduced on the ship surface and free-surface by allocating fine spacings of the grid system in the proximity of the two surfaces. Symmetry conditions are imposed on the center plane.

The turbulent kinetic energy K is set at zero on the body boundary and it is calculated by the normal procedure on the free-surface. The turbulent motion on the free-surface is important when wave breaking occurs. However, this consideration is postponed to future study. No other assumption is introduced to implement boundary conditions for the turbulent flow, although it can play an important role in particular problems.

7. Computed Results

7.1. Condition of Computation

A ship model with a simple mathematical configuration called Wigley's hull is chosen for the computation. The length of the model is 2.5 m and the offsets of the hull are expressed by the following equation:

$$Y = (L/20)\{1 - (2X/L)^2\}\{1 - (Z/d)^2\}. \tag{51}$$

Here, (X, Y, Z) are coordinates of the hull surface in the (x^1, x^2, x^3) coordinates and d is the draft of the model, which means that the depth below the undisturbed free-surface is 0.156 m in the present case.

All the coordinates and variables are made dimensionless by Eq. (35) and the reference length L (the ship length) is assumed to be unity in the subsequent description. The length, width, and depth of the initial computational domain are 2.00, 0.16, and 0.12 for the cases of a double-model-flow without free-surface and 2.00, 0.40, and 0.12 for the principal cases of a flow with free-surface. In each fluid region $170 \times 20 \times 30$ and $170 \times 30 \times 20$ grid points are allocated in the ξ^1, ξ^2, and ξ^3 directions, respectively. On one side of the hull surface 101×19 and 101×13 grid points are located as seen in Fig. 2 for the case of a double-model-flow and in Fig. 3 for the case of a flow with free-surface. The grid points are numbered by (I, J, K) for te (ξ^1, ξ^2, ξ^3) directions, respectively; for instance, the plane at $I = 30$ means an approximately vertical plane at the forward end of the hull (called FP) and one at $I = 130$ the aft end (called AP). The smallest grid spacings are approximately 0.0035, 0.0009, and 0.0031 in the x^1, x^2, and x^3 directions, respectively. The attraction and decay factors used to generate the grid system shown in Fig. 3 are listed in

TABLE III

Attraction and Decay Factors for Grid Generation

	$R = 10^3$		$R = 10^4$		$R = 10^5$	
	A	B	A	B	A	B
$\xi^1 = 30$ (FP)	30,000	0.4	30,000	0.4	30,000	0.4
$\xi^1 = 130$ (AP)	30,000	0.4	30,000	0.4	30,000	0.4
$\xi^2 = 2$ (hull-surface)	60,000	0.4	150,000	0.4	180,000	0.4
$\xi^3 = 8$ (keel)	40,000	0.5	40,000	0.5	40,000	0.5
$\xi^3 = 20$ (free-surface)	40,000	0.5	40,000	0.5	40,000	0.5

Table III. For the grid system of the double-model-flow the same values are used except for the free-surface.

The computations are performed at the Reynolds numbers (R) of 10^3, 10^4, and 10^5 and at the Froude numbers (F) of 0.170, 0.200, and 0.289. Both parameters are based on the length of a ship L and the uniform speed of advance U. The SGS turbulence model is not used in the computations at $R = 10^3$. The time increment is 3.33×10^{-4} dimensionless time, which is determined by the stability consideration with respect to Courant and diffusion numbers, since an explicit scheme is used. The flow velocity is linearly accelerated for 1000 time steps (0.333 dimensionless time) and the computation is continued to the 2000th or 3000th time step when an almost steady state is reached.

The number of iterations necessary to generate the new grid system by solving Eq. (3) is usually less than three, and that for solving the Bernoulli quantity field by Eq. (41) is about ten.
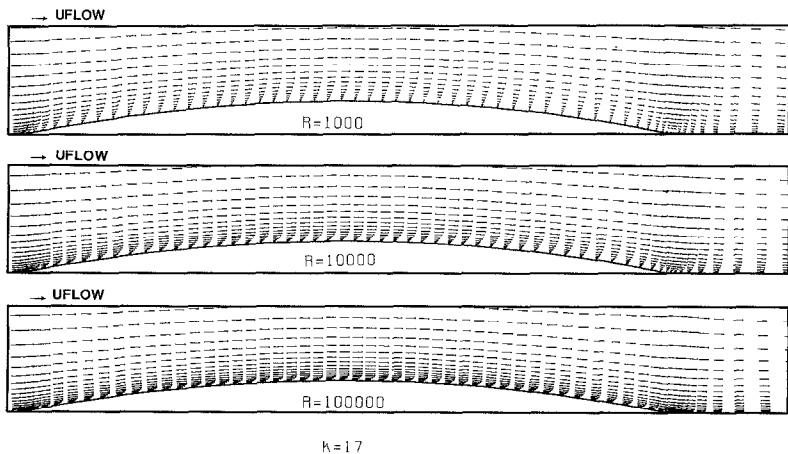

FIG. 4. Velocity vector fields on a x^1–x^2 coordinate surface computed by the double-model-flow assumption at $R = 10^3$, 10^4, and 10^5.
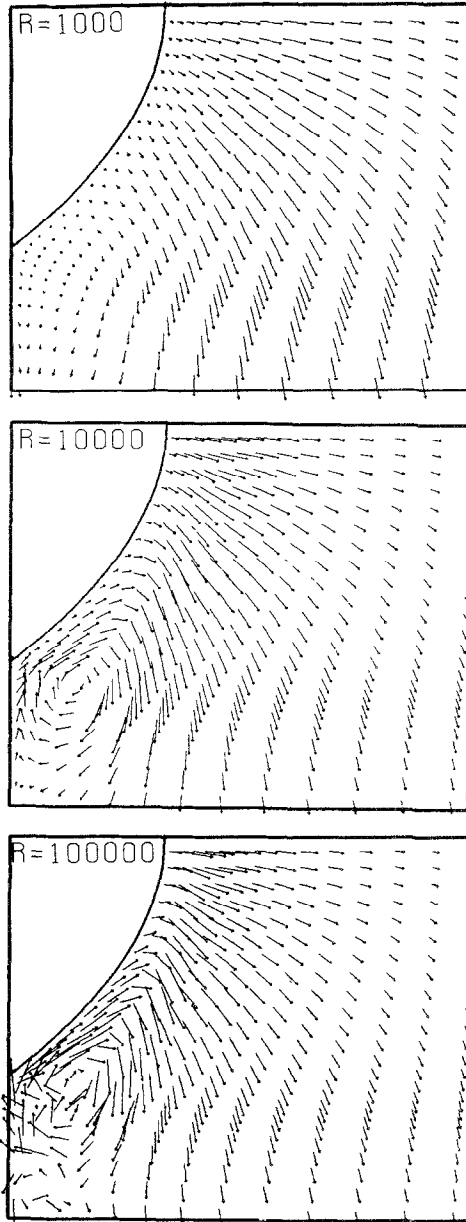
FIG. 5.   Velocity fields on a x^2–x^3 coordinate surface at $I = 60$ computed by the double-model-flow assumption at $R = 10^3$, 10^4, and 10^5.

7.2. *Effect of Reynolds Number*

Velocity vector fields on typical coordinate surfaces are compared in Figs. 4 and 5. One velocity vector is drawn for each double spacing in the ξ^1-direction in Fig. 4 and all the vectors are drawn in Fig. 5. The thickness of the boundary layer is reduced with the increasing Reynolds number. It is also noted that the vortex caused by flow separation is obscure at $R = 10^3$, while, on the contrary, the velocity vectors show fluctuation in the vortical region at $R = 10^5$. The former is attributable to the excessive viscosity and the latter to insufficient resolution. The magnitude of the term derived from the turbulence model is of the same order as the term of the molecular viscosity in the vicinity of the body surface at $R = 10^4$. The turbulence model plays a more important role at $R = 10^5$ and it will extend the availability of the present method to the higher Reynolds number provided sufficiently fine grid spacing can be used.

The grid spacing of the present method becomes relatively coarser at a little distance from the ship surface, where an attached vortex causes a complicated flow field. Although this problem will be resolved by using a larger number of grids, it is restricted by the storage limitation of the computer presently available. Therefore, subsequent computations are carried out at $R = 10^4$.
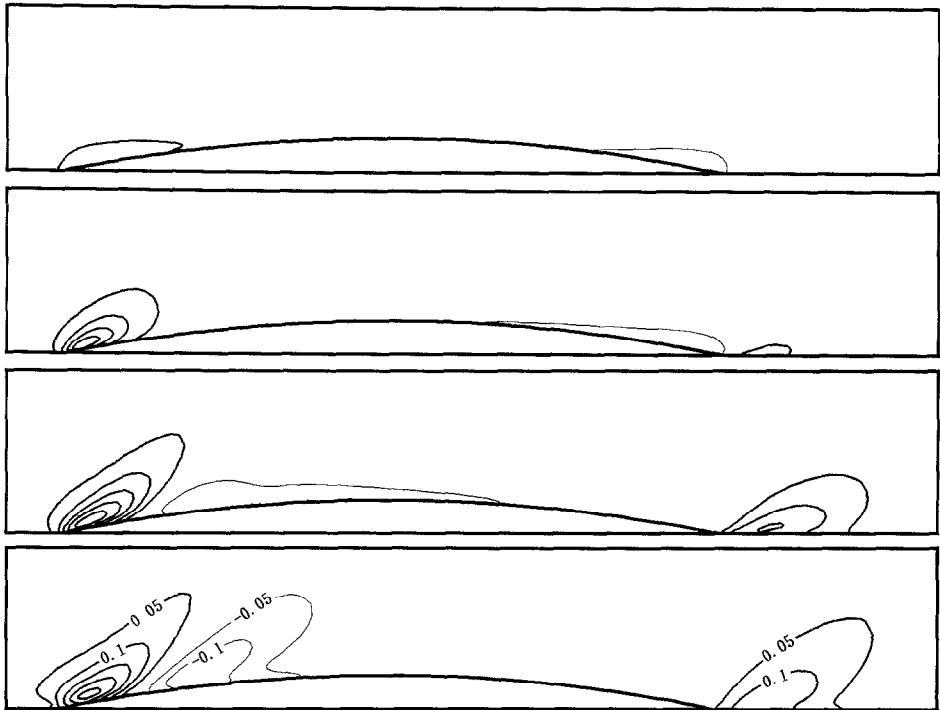

FIG. 6.   Time sequence of waves for $F = 0.289$ and $R = 10^4$ at $T = 0.167, 0.333, 0.500$, and 0.667; the ship model is accelerated for the period of 0.333; the contour interval is $0.05\ U^2/2g_r$; and positive values are drawn in bold lines.

7.3. *Wave Formation and Pressure Distribution on a Ship's Surface*

The time sequential development of the waves about a ship is shown in Fig. 6 for the case of $F = 0.289$, which shows that an almost steady state is attained at the time of 0.667 after 2000 steps of time-marching. It is noted that the wave height is made dimensionless with respect to the head of a uniform stream $U^2/2g_r$.

The variation of bow and stern waves due to the difference of the Froude number is shown in Fig. 7. It indicates that the wavelength is increased and the angle of the wave crest line to the centerline is reduced by the increasing Froude number (involving the decrease of the maximum dimensionless wave height), the latter of which is one of the typical characteristics of the free-surface shock wave [1]. The maximum wave height at $F = 0.289$ is $0.28 \times U^2/2g_r$, while the measured contour map shows the maximum wave height of $0.35 \times U^2/2g_r$ [7]. At present the degree of accuracy is not superior to the previous TUMMAC-IV method that uses an inflexible rectangular cell system. This is due mostly to the coarser grid spacing on the uppermost coordinate surface and in its neighborhood.

Figure 8 compares the pressure distribution on the ship surface for $R = 10^3$ and 10^4 and also with the measured pressure distribution, in which the hydrostatic pressure is excluded. The values on the contour lines correspond to the pressure coefficient. By increasing the Reynolds number up to 10^4, the agreement in the phase of the bow wave seems to be improved, and the presence of positive pressure at the aft end is particularly interesting, since it seems to be influenced by the interaction of waves with the viscous flow. However, the maximum pressure at the bow for $R = 10^3$ apparently shows better agreement with the measured value than for $R = 10^4$. This is attributable to the higher wave height at the lower Reynolds number, since the maximum wave height is 40% of the head of the uniform stream at $R = 10^3$ while it is 28% at 10^4 and 35% in the experiment at $F = 0.289$. This does not imply a better degree of accuracy for the lower Reynolds number. By improving the accuracy, the wave height will be raised by a higher Reynolds number and consequently the pressure contour will show better agreement with the larger magnitude.

7.4. *Flow Field*

Velocity vector fields on six vertical coordinate surfaces, which are not plane but slightly curvilinear, are shown in Fig. 9 for the case of a double-model-flow and for

observed. The generation of large-scale vortices by three-dimensional separation is well simulated. The dominant vortex on the fore part has clockwise rotation and that on the after part, anticlockwise rotation. These vortices having axes along the x^1-direction are called bilge vortices in the field of naval architecture. However, in the present case of a Wigley's hull that does not have a bilge (a round corner at the bottom side of a hull with square-shaped cross sections) these separated vortices are generated by the downward and upward flows around the fore and after parts,
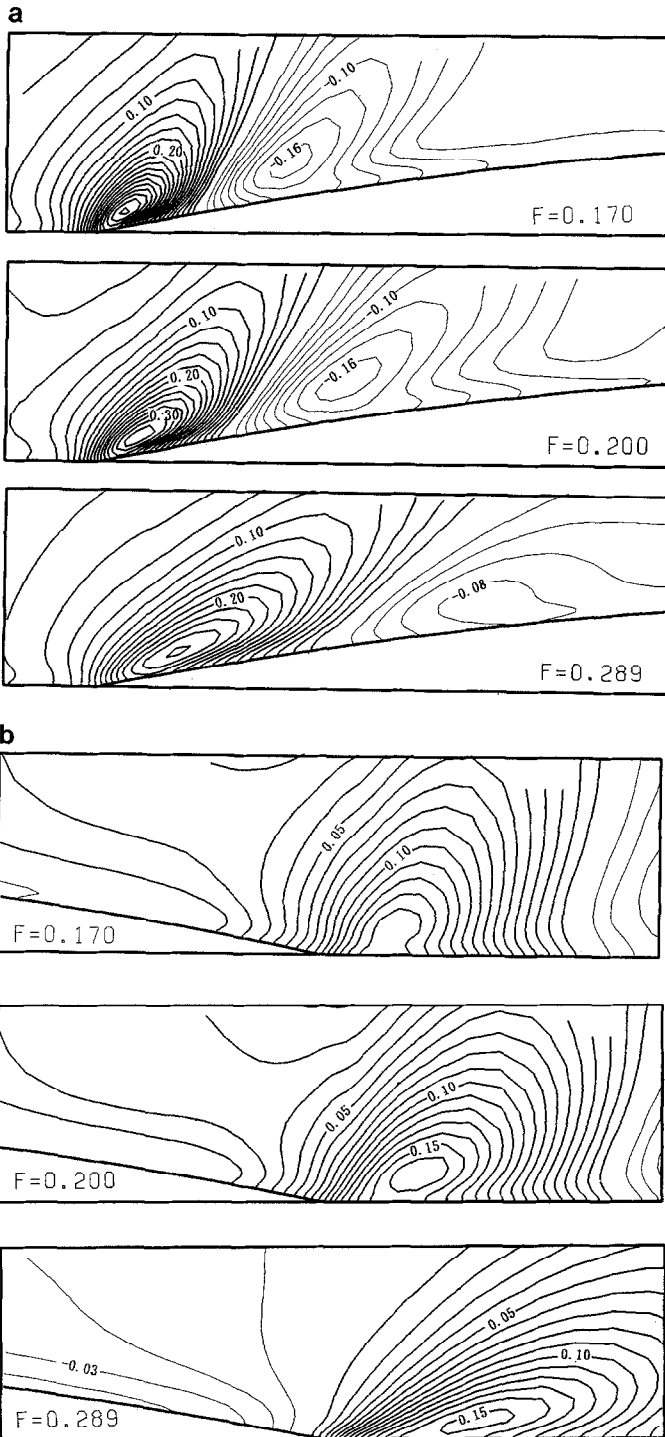
FIG. 7(a). Contour maps of bow waves at $F = 0.170$, 0.200, and 0.289 and $R = 10^4$; the contour interval is 0.02 $U^2/2g_r$; and positive values are drawn in bold lines. (b) Contour maps of stern waves with the same conditions as Fig. 7(a); the contour interval is 0.01.
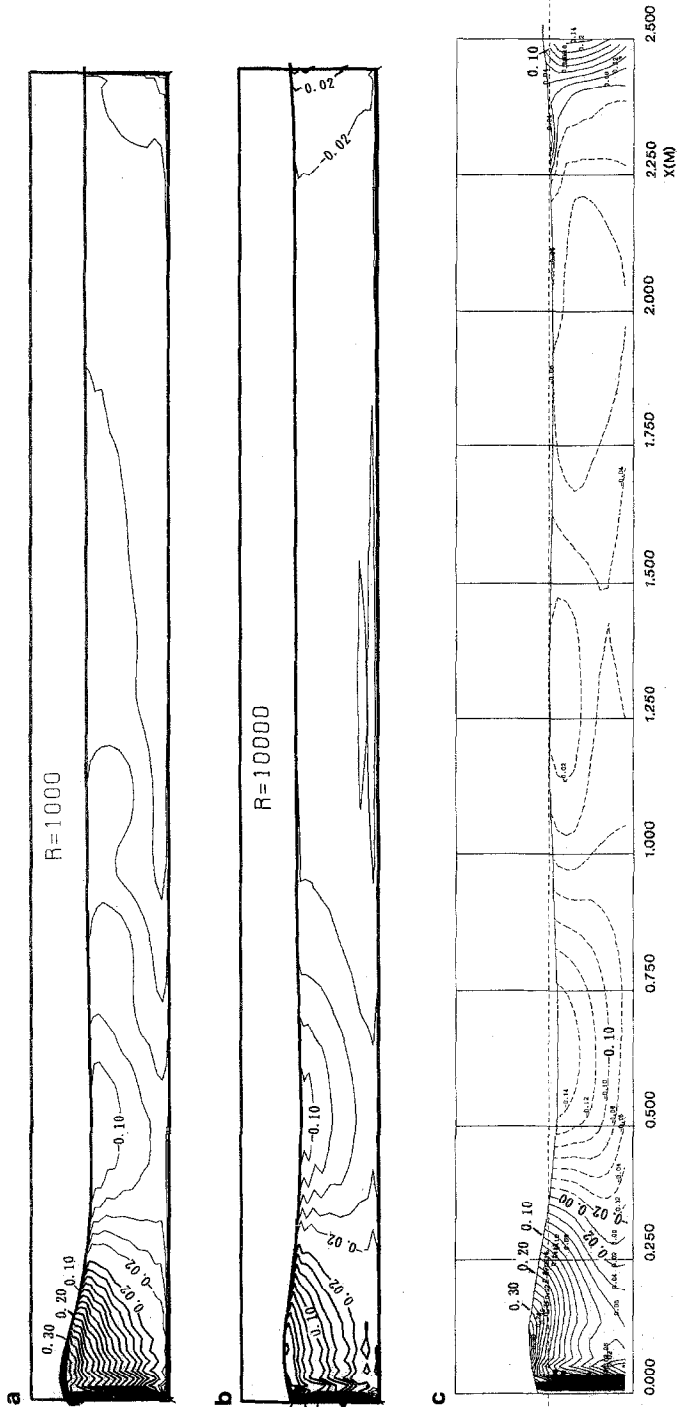
FIG. 8. Pressure distribution on the hull surface at $F = 0.289$: (a) computed at $R = 10^3$; (b) computed at $R = 10^4$; and (c) measured.
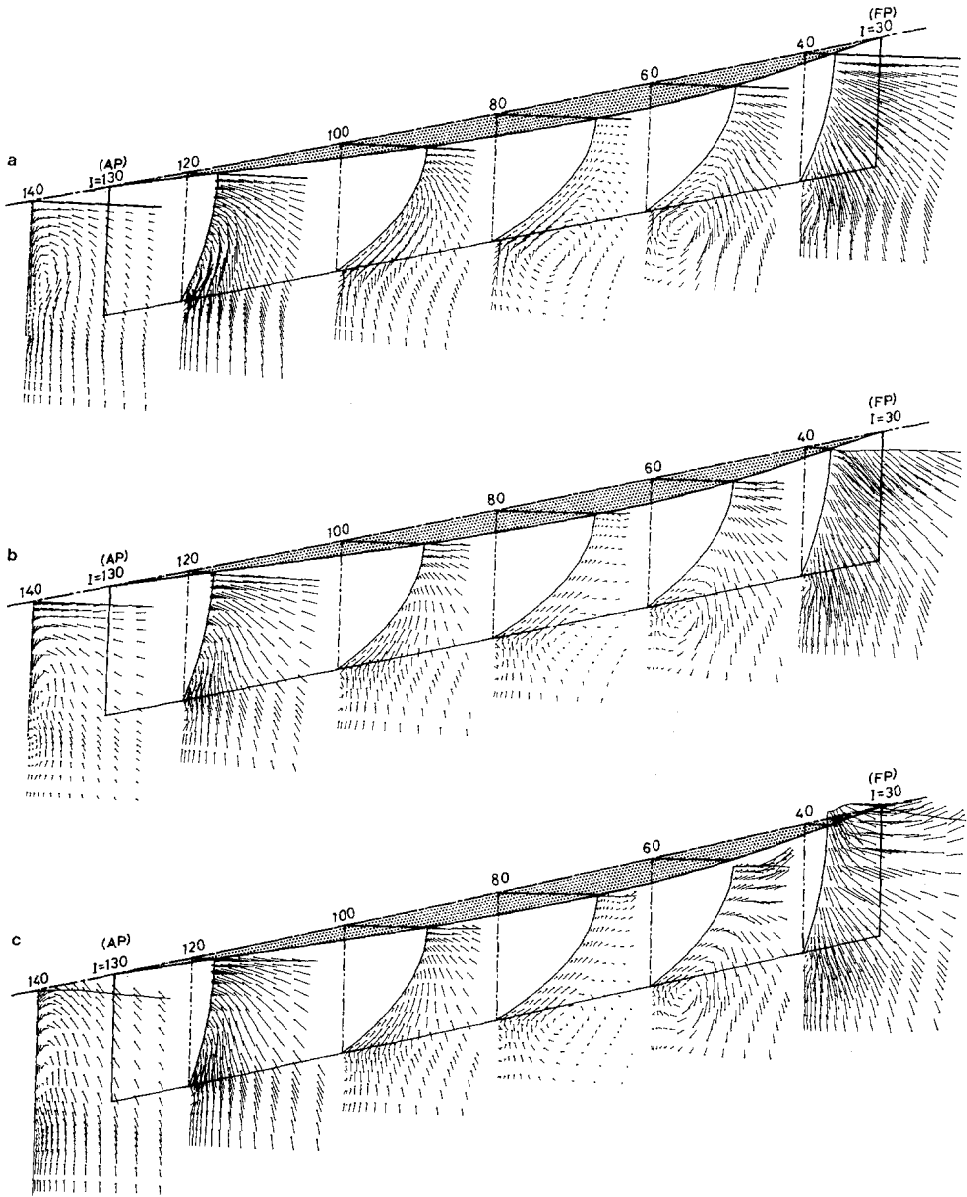
FIG 9(a). Velocity vector field at: $F = 0.0$, $R = 10^4$; (b) $F = 0.17$, $R = 10^4$; (c) $F = 0.289$, $R = 10^4$.

respectively, which are proper consequences of the longitudinal variation of the displacement of a ship.

Contour maps of a velocity component u^3 and vorticity component ω^1 about a longitudinal axis and pressure coefficient excluding the hydrostatic pressure are shown in Figs. 10 to 12, where comparison is made between the double-model-flow case and the highest Froude number case. Since three longitudinal locations $I = 40$, 60, and 140 where wave motions are prominent are chosen, the effect of wave motion on the flow field is quite obvious. The highest value of downward velocity in Fig. 10(a) is not varied by the wave motion, but the geometry of the contour is obviously deformed by the presence of upward and downward velocities on the free-surface. The wake field behind a ship shown in Fig. 10(c) also shows a remarkable difference due to the wave motion. Similarly, the vorticity field is quite deformed by the wave motion. Anticlockwise rotation with large magnitude is generated near the free-surface as shown in Fig. 11(a). Then, the clockwise vorticity region is pulled upward by the wave motion at $I = 60$ in Fig. 11(b), and the width of the voriticity region with anticlockwise rotation is narrowed in the wake as shown in Fig. 11(c). The influence of the wave motion is most remarkable in the pressure field shown in Fig. 12. This seems to be quite reasonable, since this difference of pressure leads to wave resistance which is not related to a ship in a double-model-flow. This pressure field caused by the wave motion is supposed to give influences on the viscous flow including the three-dimensional separation noted in Fig. 11.

The longitudinal variation of the vorticity (ω^1) contour map is shown in Fig. 13 for the case of the highest Froude number. This figure shows the evolution of vortices with longitudinal axes which are mostly caused by three-dimensional separation. Excluding the vortex with anticlockwise rotation near the fore end closely beneath the free-surface, the most dominant vortices are one with the clockwise rotation about the fore part of the hull and one with anticlockwise rotation about the after part, which has been widely known since the work by Tagori [15]. It seems that the present simulation elucidates that a vortical layer with anticlockwise rotation already starts to develop on the ship surface of the fore part. This anticlockwise vortex motion on the fore part seems to be generated by the influence of the attached vortex with clockwise rotation which causes an upward flow on the ship surface. In a sense, a kind of pairing motion of an attached vortex with another one having opposite sign is present along the ship's length. This pairing motion is similar to the phenomenon observed in the vortex shedding of a circular cylinder placed in an oscillatory flow at a low Keulegan–Carpenter number [16]. The shed vortex in this oscillatory flow remains in the proximity of the cylinder, again attaches to the cylinder surface and gives significant effect on the flow separation to the opposite direction in the next half cycle. The downward and upward flows along the fore and after parts of a ship surface seem to play the role of the oscillatory flow. This figure indicates the need for the present method to understand this complicated pairing motion of vortices as well as the interactions with the waves.
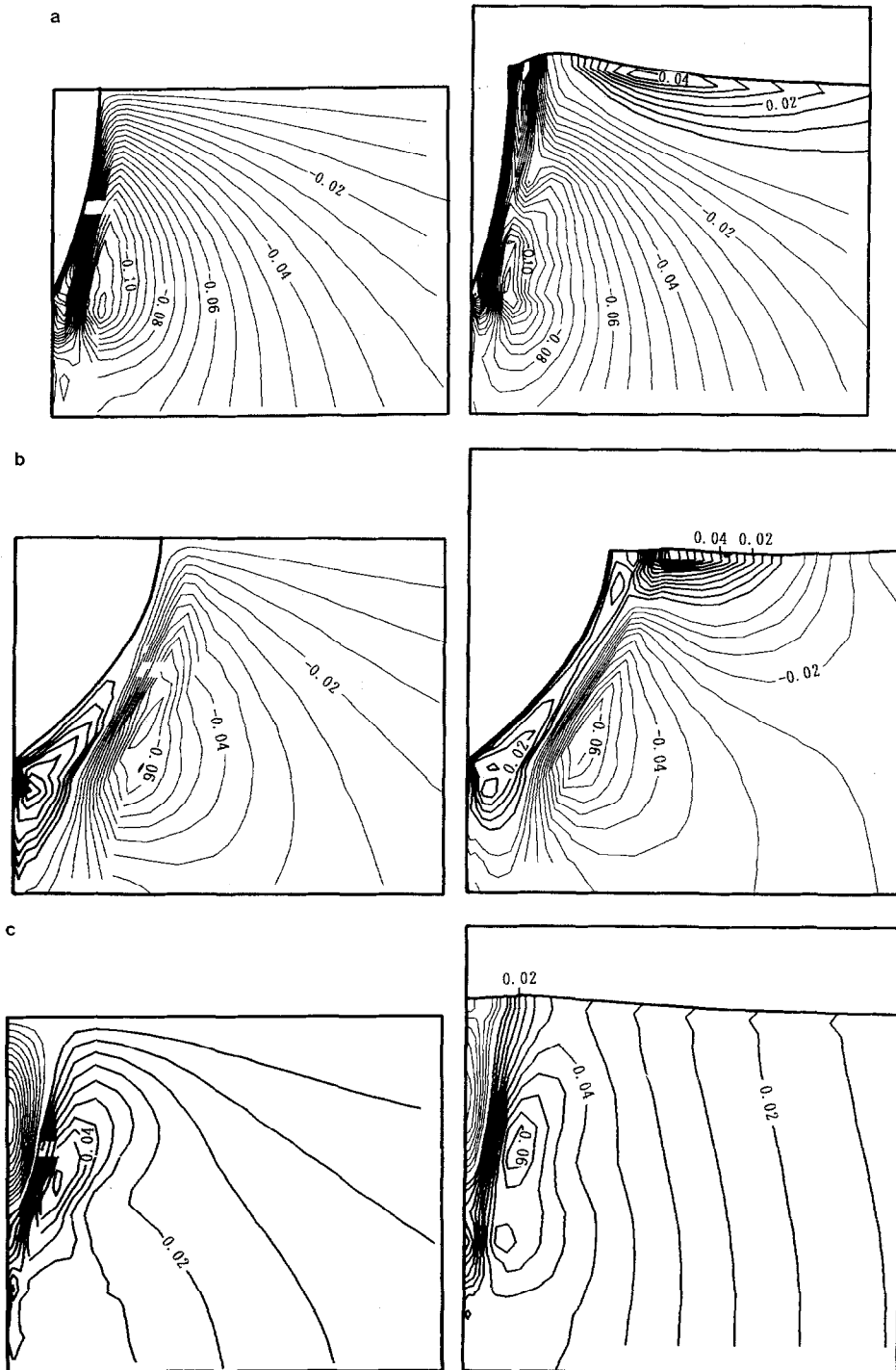
FIG. 10(a). Contour map of u^3 at $I=40$, left; double-model-flow, right; $F=0.289$, the contour interval is 0.005, and the upward velocity is drawn in bold lines. (b) At $I=60$. (c) At $I=140$.
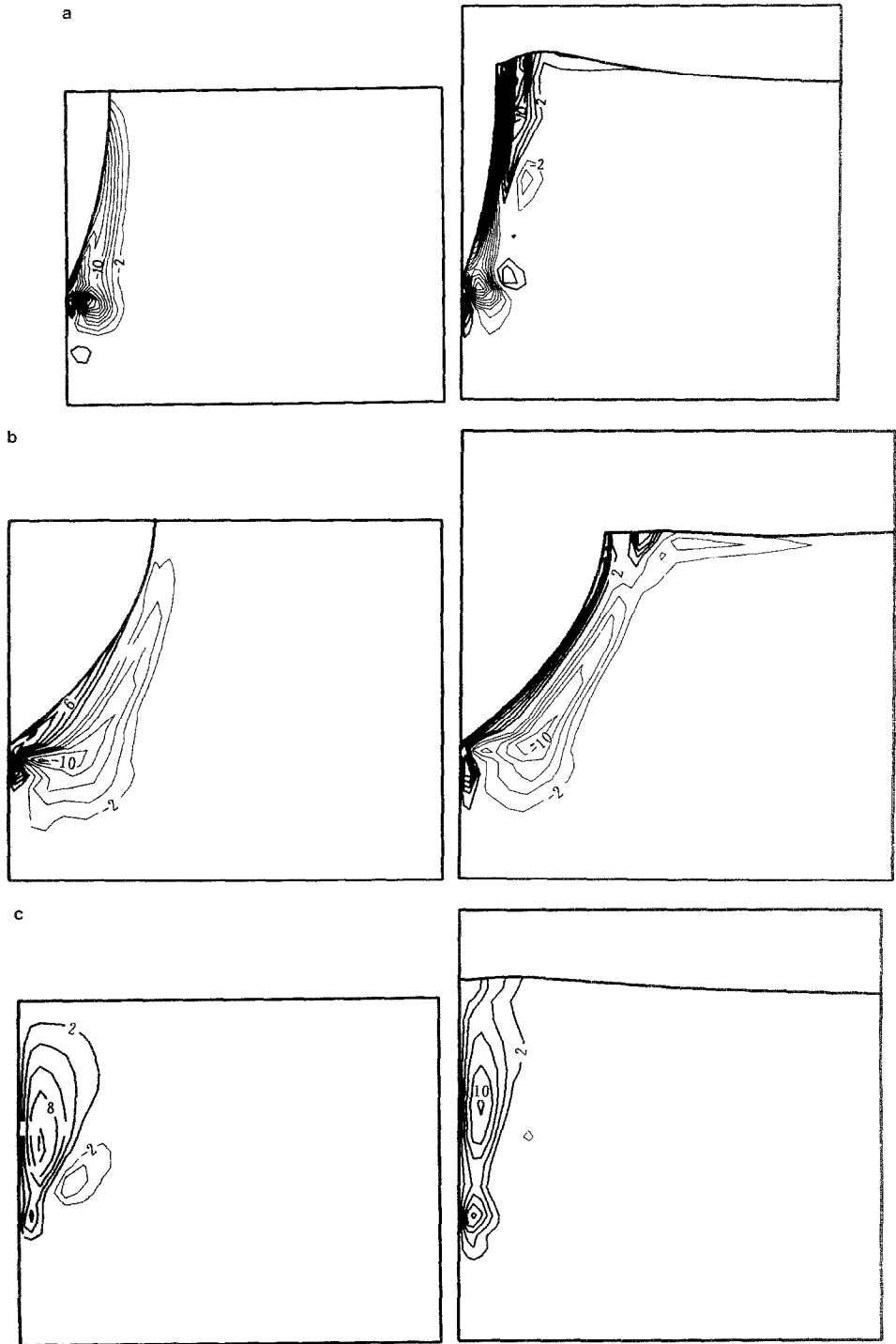
416

FIG. 11(a). Contour map of ω^1 at $I = 40$, left; double-model-flow, right; $F = 0.289$, the contour interval is 2, and the anticlockwise vorticity is drawn in bold lines. (b) At $I = 60$. (c) At $I = 140$.
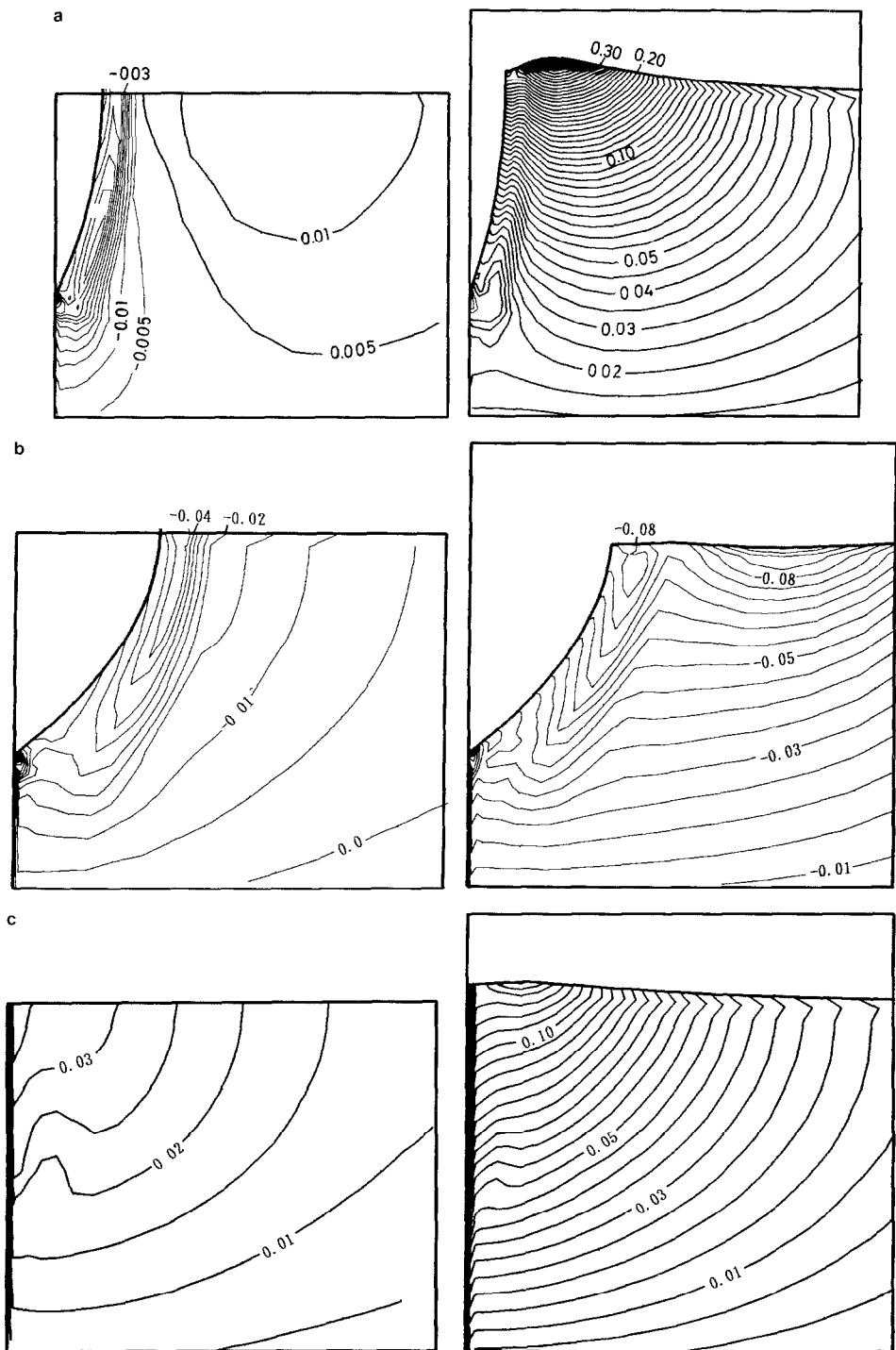
417

FIG. 12(a). Contour map of P at $I = 40$, left; double-model-flow, right; $F = 0.289$, the contour interval is 0.005, and the positive pressure is drawn in bold lines. (b) At $I = 60$. (c) At $I = 140$.
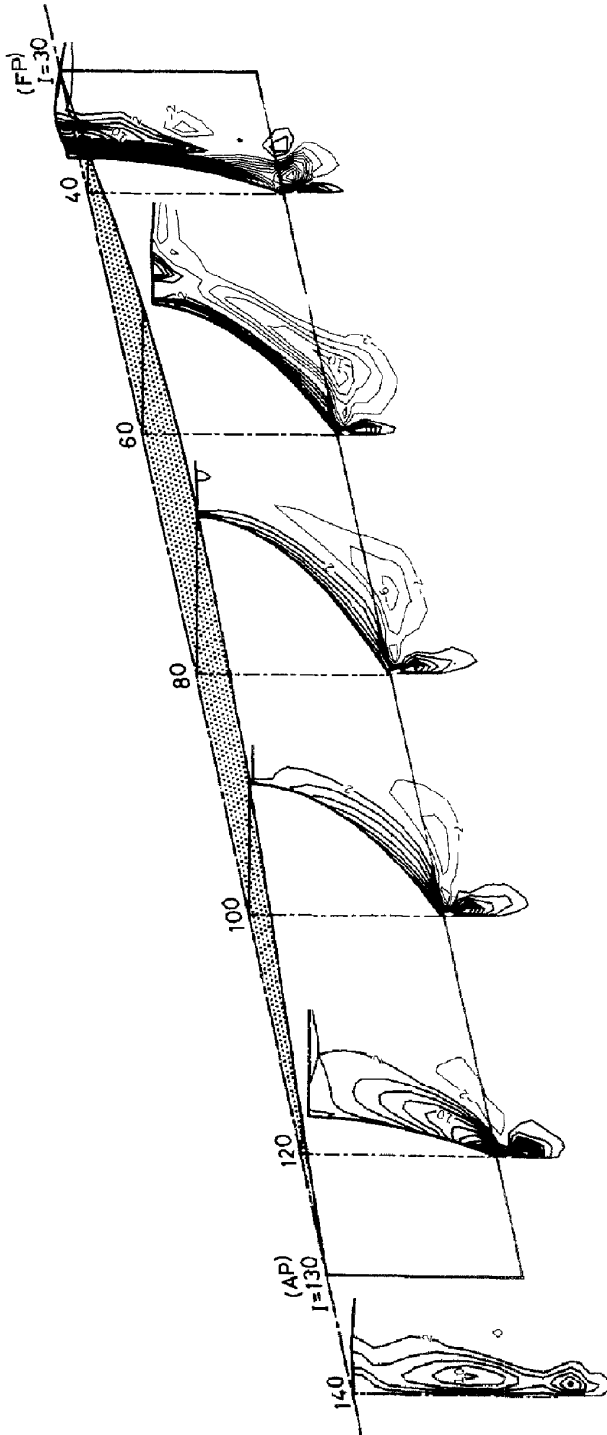
Fig. 13. Contour map of ω^1 at six locations for $F = 0.289$ and $R = 10^4$; the interval of contours is 2 and the anticlockwise rotation is drawn in bold lines.

8. CONCLUDING REMARKS

The present method seems to have succeeded in simulating large-scale vortical flows, wave motions, and their interactions, although the Reynolds number is limited to 10^4. The theoretical tools so far developed have found difficulty in the detailed explanation of the complicated large-scale vortical flow about an advancing ship. The present method and improved versions will cultivate a new research field of ship hydrodynamics. The principal concept and algorithm are similar to the so-called large-eddy simulation in many respects. By raising the degree of resolution with larger computer storage, together with improved techniques, more detailed viscous fluid motion interacting with wave motion will be simulated at higher Reynolds numbers, at which the SGS turbulence model will play a more important role in the future.

The required degree of accuracy depends on the purpose of the simulation. For scientific purposes the degree of accuracy for the resolution of delicate physical phenomena is of significant importance, and for engineering purposes the accuracy in the estimated forces, which are consequences of fluid motion, is of practical importance. For both purposes qualitative resemblance of the flow field between experiments and computations is of limited importance. The efforts must be continuously focused on the achievement on an adequate degree of accuracy. In the problem of resistance to a moving body, in particular, the estimation is often very difficult, since it is derived by subtracting a force on the after part from that on the fore part. Besides the complicated phenomena of flow separation, wave generation and their interactions play certain roles. It is hoped that the improved version of the present method with better properties of accuracy, stability, and economy will become a useful tool for this purpose in the future.

The computer code called WISDAM for wave and viscous flows was recently developed at the Experimental Tank Laboratory of the University of Tokyo. The first version WISDAM-I was applied to viscous flows about a circular cylinder in steady and oscillatory motions [16], and the second version WISDAM-II, to a flow about a ship is described in this paper. These computer codes are composed for a supercomputer, namely for a vector processor, HITAC S-810/20 of the Computer Center of the University of Tokyo, and almost 100% of the computation is performed by the vector processor. However, since the degree of optimization in the coding for the vector processor was not satisfactory in the WISDAM-I, it is remarkably improved in the WISDAM-II. The CPU time is reduced to about one third. For the computation of 3000 time steps at $R = 10^4$ and $F = 0.289$ the CPU time was about 40 min by the above supercomputer.

REFERENCES

1. H. MIYATA AND T. INUI, *Adv. Appl. Mech.* **24**, 215 (1984).
2. Y. DOI *et al.. J. Soc. Nav. Archit. Japan* **150**, 30 (1981).
3. Y. DOI *et al., J. Soc. Nav. Archit. Japan* **151**, 23 (1982).
4. H. C. CHEN AND V. C. PATEL, IIHR Report 285, Institute of Hydraulic Research, The University of Iowa, Iowa, 1985.
5. Y. KODAMA, in *Proceedings of the Symposium of Fluid Dynamic Drag, Soc. Nav. Archit., Japan,* 1985, 29. [Japanese]
6. H. MIYATA, S. NISHIMURA, AND A. MASUKO, *J. Comput. Phys.* **60**, No. 3, 391 (1985).
7. H. MIYATA AND S. NISHIMURA, *J, Fluid Mech.* **157**, 327 (1985).
8. J. W. DEARDORFF, *J. Fluid Mech.* **41**, 453 (1970).
9. J. SMAGORINSKY, S. MANABE, AND J. L. HOLLOWAY, *Mon. Weather Rev.* **93**, 727 (1965).
10. J. F. THOMPSON *et al., J. Comput. Phys.* **15**, 299 (1974).
11. C. W. MASTIN AND J. F. THOMPSON, *Numer. Math.* **29**, 397 (1978).
12. S. P. SHANKS AND J. F. THOMPSON, in *Proceedings of the 2nd Intern. Conf. on Numerical Ship Hydrodynamics, Berkeley,* 1977, edited by J. V. Wehausen and N. Salvesen (David Taylor Naval Ship R & D Center), 202.
13. Z. U. A. WARSI, *AIAA J.* **19**, 240 (1981).
14. M. S. LONGUET-HIGGINS AND E. D. COKELET, *Proc. R. Soc. London A* **350** (1976), 1.
15. T. TAGORI, in *Proceedings of the 11th Intern. Towing Tank Conf. Tokyo.* 1967.
16. N. BABA AND H. MIYATA, *J. Comput. Phys.* in press.
17. H. MIYATA, *J. Comput. Phys.* **65**, 179 (1986).
18. S. A. ORSZAG AND M. ISRAELI, *Ann. Rev. Fluid Mech.* **6**, 281 (1974).